Organic Photonics and Photovoltaics
Research Article • DOI: 10.2478oph-2013-0003 • OPP • 2013 • 24-38

VERSITA

Improving the layer morphology of solution-processed perylene diimide organic solar cells with the use of a polymeric interlayer

Abstract

Herein we demonstrate a method to improve the power conversion efficiency (PCE) parameter of organic photovoltaic (OPV) devices based on the electron acceptor N,N'-bis(1-ethylpropyl)-perylene-3,4,9,10-tetracarboxylic diimide (PDI) blended with the electron donor poly(indenofluorene)-aryl-octyl (PIF-Aryl). The device parameters of the short-circuit current, open-circuit voltage and fill factor are found increased after the insertion of a thin poly [9, 9-dioctylfluorene-co-N-[4-(3-methylpropyl)]-diphenylamine] (TFB) photoactive interlayer between the hole-collecting electrode and the photoactive layer of the device. Unlike to most of the cases where interlayers serve as charge extractors, in our system the polymeric interlayer serves as a morphology modifying agent that drives the PDI component to segregate better at the interface with the device cathode; that is at the carrier-collecting electrode interface, which is not in physical contact with the interlayer. The processes of energy/charge transfer of the TFB excitons to/with the PIF-Aryl:PDI top-layer are also addressed. Charge transfer reactions dominate at the TFB/PIF-Aryl:PDI interface but no significant contribution in the photocurrent generation is seen in the photoaction spectra of the bilayer device.

Ranbir Singh[1], Marta M. Mróz[2], Fabio Di Fonzo[1], Juan Cabanillas-Gonzalez[2], Enrico Marchi[3], Giacomo Bergamini[1,3], Klaus Müllen[4], Josemon Jacob[5], Panagiotis E. Keivanidis[1]*

1 *Centre for Nanoscience and Technology@PoliMi, Fondazione Istituto Italiano di Tecnologia, Via Giovanni Pascoli 70/3, 20133 Milano, Italy*

2 *Instituto Madrileño de Estudios Avanzados en Nanociencia (IMDEA-Nanociencia), c/Faraday 9, Cantoblanco, 28049, Madrid, Spain*

3 *Department of Chemistry "G. Ciamician" University of Bologna, Via Selmi 2, 40126 Bologna, Italy*

4 *Max-Planck Institute for Polymer Research, Ackermannweg 10, D-55128, Mainz, Germany*

5 *Centre for Polymer Science & Engineering, Indian Institute of Technology Delhi, New Delhi 110016, India*

Received 06/15/2013
Accepted 07/17/2013

Keywords

PACS:

1. Introduction

During the last decade the field of organic photovoltaic (OPV) devices has progressed significantly and power conversion efficiencies (PCE) have been reported in the order of 10% [1–4]. The rapid improvement in the PCE values of the most efficient OPV devices has been achieved mainly by the development of photoactive layers based on a new generation of electron donating polymers, which have the ability to absorb at a wider spectral range towards lower photon energies, mixed with electron accepting fullerene derivatives [5–7]. The OPV devices of these polymeric composites exhibit increased photocurrent generation efficiencies [5]. In parallel to the production of next generation polymeric donors with optimized light harvesting capabilities much progress has been achieved also in understanding the role of photoactive layer morphology in the charge generation and charge extraction efficiencies [8–12]. Several reports have demonstrated efficient photo-induced charge transfer between the donor/acceptor pair not necessarily guarantee a high short-circuit (Isc) current in the OPV device [13]. High fill factor values of OPV devices are obtained when the distribution of the donor and the acceptor components across the photoactive layer favours the extraction of the photogenerated carriers at the corresponding carrier-collecting electrode. In addition, appropriate photoactive layer morphologies are required for optimizing the distribution of the donor and acceptor components across the device electrodes. The optimization of the phase separated components in the photoactive layer across the device contacts

*E-mail: pekeivan@iit.it

can also minimize the injection of carriers from the device electrodes to the components of the photoactive layer. Efficient blocking of carrier injection result in the minimization of device dark current (I_d). and consequently this can improve the device open-circuit voltage (V_{oc}) [14, 15].

The issues of poor charge generation efficiency and charge extraction become more important for the case of organic solar cells that are based on non-fullerene electron acceptors [16, 17]. Despite the growth of interest in the development of non-fullerene containing power generating devices, this type of device still exhibit much lower power conversion efficiencies than those of the fullerene-based OPVs.

In this work we show how the insertion of a solution-processed interlayer [18, 19] in a non-fullerene-based OPV device can contribute to the improvement in the morphology of the photoactive layer and in the photocurrent generation efficiency of the device. Previous reports on the effect of inserting interfacial layers in fullerene-containing OPV device structures [20, 21] have shown the beneficial effect of those interlayers in the overall device efficiency both for the case of conventional and inverted device geometries. Some types of interlayers improve charge extraction at the interlayer/photoactive layer interface [14, 22, 23]. Other types serve as optical spacers for improve the absorption of the incoming light without increasing the thickness of the photoactive layer [24]. Interlayers may also be used for selectively tuning the work function of the electrode on which they are deposited [25, 26].

At present we focus our attention on the effects of an interlayer in the film morphology a non-fullerene based OPV composite layer and based on spectroscopic studies we evaluate the impact of the active layer morphology modification on the process of exciton dissociation and charge generation. Recent studies in inverted fullerene-based OPV cells suggested that the use of interlayers can change the morphology of the photoactive layer so that the domains of the donor and the acceptor components can be reduced and the donor/acceptor interfacial area can be increased for favouring the photocurrent generation efficiency of the OPV device [27]. In addition, it was proposed that the use of interlayers in OPV can cause charge transfer reactions between the photoactive layer and interlayer components that lead to improved photocurrent generation efficiencies [28].

In our work we study OPV devices with photoactive layers consisting of the electron donor poly(indenofluorene)-aryl-octyl (PIF-Aryl) and the electron acceptor N,N'-bis(1-ethylpropyl)-perylene-3,4,9,10-tetracarboxylic diimide (PDI). PDI derivatives have been used previously as electron acceptors in photocurrent generation devices. Nevertheless, no control has been yet achieved in the degree at which PDI aggregates for positively influencing the process of charge transport. Ideally, PDI aggregation should take place without leading to the recombination and the trapping of charges in large PDI domains [29, 30]. The use of an interlayer for gaining control over the tendency of PDI to aggregate is a smart methodology for the development of optimized PDI-based OPV composites. PIF-Aryl is an amorphous [31] polymeric matrix that has been previously proposed for the development of organic light-emitting diodes (OLEDs) [32] and organic lasers [33]. In our study, the amorphous matrix of PIF-Aryl polymer simplifies the control of PDI aggregation in the solid state of a bulk heterojunction blend and serves as an appropriate photoactive polymeric host for the establishment of a correlation between PDI aggregation and photocurrent generation in PDI-based solar cells [34]. For improving the performance of the PIF-Aryl:PDI devices we make use of the solution processable [9, 9-dioctylfluorene-co-N-[4-(3-methylpropyl)]-diphenylamine] (TFB). A very thin TFB layer is inserted by spin-coating between the PEDOT:PSS hole-collecting layer and the photoactive layer of PIF-Aryl:PDI. TFB was previously utilized for improving the device performance of OLEDs and organic photodetectors [18, 19, 35, 36]. Also for the case of OPVs the use of a cross-linked TFB interlayer was found to improve the device efficiency of fullerene-based OPVs due to an improved fill-factor (FF) parameter and to a reduction in the device dark current (I_d) that increased the open-circuit voltage (V_{oc}) [14].

Based on the spectroscopic and the electrical characterization experiments we investigate in detail whether the efficiency of charge transfer between the TFB interlayer and the PIF-Aryl:PDI active layer correlates to the photocurrent generation efficiency of the corresponding TFB/PIF-Aryl:PDI device. We conclude that no significant charge transfer reactions take place at the TFB/PIF-Aryl:PDI interface but an enhancement is observed in device photocurrent efficiency of the bilayer in respect to the single-layer control device. Photoluminescence spectroscopy, transient absorption spectroscopy, electrical characterization and high resolution scanning electron micriscopy studies of the PIF-Aryl:PDI and TFB/PIF-Aryl:PDI systems suggest that the deposition of the TFB interlayer on the hole-collecting device electrode (bottom contact of PEDOT:PSS,) produces a morphology that optimizes the device performance. In the presence of TFB the PDI component forms aggregates adjacent to the electron-collecting device electrode (top contact of Al). This improvement in morphology helps the extraction of the photogenerated carriers at the device electrodes. In addition, the I_d parameter of the TFB/PIF-Aryl:PDI device is found

reduced.

2. Experimental Section

2.1. Materials

The synthetic protocol of the PIF-Aryl derivative has been described before [32]. Based on GPC (THF, poly(para-phenylene) standards) the molecular weight is M_n = 6.64 104 g/mol and the polydispersity index is D= 3.86. PDI and TFB were purchased from Solarmer Energy Inc. and American Dye Source Inc. respectively and they were used as received.

2.2. Solar cell fabrication and characterization

Single and bilayer solar cell devices were fabricated on commercially available glass/ITO substrates (15 Ω/□). The ITO coated glass substrate was ultrasonically cleaned using acetone and isopropanol for 15 minutes. After preliminary cleaning, substrates were cleaned with Hellmanex III to remove contaminants and residues from the surface of ITO. The Substrates were again cleaned with DI water followed by acetone and isopropanol for 15 minutes and they were placed in oxygen plasma (100 W) for 10 minutes. Then a layer of poly(3,4-ethylenedioxythiophene)–polystyrene sulfonic acid (PEDOT:PSS) was spin coated over the ITO. The glass/ITO/PEDOT:PSS layers were dried in air at 140°C for 30 minutes. Then TFB solution of concentration with 2 mg/ml in toluene was spin coated over PEDOT:PSS layer, which was subsequently dried in nitrogen ambient at 150°C for 30 minutes. The solutions of PIF-Aryl: PDI blend with 60 wt% of PDI was prepared in $CHCl_3$ solvent and the PIF-Aryl:PDI blend film was spin coated over the TFB layer. The samples were then transferred in a N_2-filled glove box and aluminum (Al) layers were deposited by thermal evaporation in vacuum (1×10^{-5} m bar) onto the active layer. Devices of 5.25 mm^2 active area were defined during the evaporation of Al through a shadow mask. Finally the devices were encapsulated with degassed epoxy and glass slides of 1 mm thickness in to the glovebox. The final structure of the OPV device was Glass/ ITO (140 nm) /PEDOT: PSS (40 nm)/ TFB (8 nm)/ PIF-Aryl: PDI (96 nm)/ Al (90 nm)/encapsulated glass. All thin film thicknesses were determined by using Dektak profilometer. The electrical characterization of single PIF-Aryl: PDI layer and TFB/PIF-Aryl: PDI bilayer devices are performed by means of external quantum efficiency (EQE), dark current-voltage (I_d-V) characteristics and by determining the basic photovoltaic parameters under simulated (AM1.5G) solar illumination. For preparing annealed devices the annealing step was performed with the use of a hot plate in a temperature between 90°C – 100°C after the deposition of the metal cathode 30 min in the N_2-filled glovebox. The samples were then transferred onto a metallic gold surface for immediate cooling.

2.3. Time integrated absorption and photoluminescence spectroscopy

Thin films of as-spun and annealed single and bilayers were prepared in an identical fashion like for the case of the active layers of the solar cell devices. UV-Vis absorption and photoluminescence spectra of the produced films were recorded with a Perkin Elmer, Lambda1050 spectrometer and a Horiba Jobin Yvon NanoLog spectrofluorimeter, respectively.

2.4. cw-PIA and µs-transient absorption

Samples for the cw-PIA and µs-TA mesurements were deposited onto quartz substrates and they were sealed in a N_2-filled glovebox with epoxy glue and glass caps in order to avoid photodegradation effects during the measurement. For cw-PIA measurements was provided by a diode pumped solid state laser (Roithner Laser Technik GmbH) at 532 nm with the maximum output power of 100 mW. The laser beam was mechanically modulated at 280 Hz. The pump intensity was adjusted by positioning neutral density filters of different optical density across the optical path. Continuous probe light was provided by a tungsten halogen lamp. Both pump and probe were focus on the sample. The light was selected by 1/8 monochromator (Cm110 Spectral Products) equipped with two gratings (600 l/mm) for visible and near-IR spectral range. Detection of the signal was carried out with a Si photodiode coupled to a dual channel lock-in amplifier (SR830, Stanford Instruments). For µs-transient absorption measurements excitation was provided by the tripled frequency output of a passively Q-switched Nd:Y:LiF laser from TEEM Photonics (355 nm, 300 ps, 1 kHz repetition rate). The pump power was adjusted with neutral density filters. Probe light was provided by a 970 nm LED source (Roithner Laser Technik) that was collimated and spatially overlapped with the pump on the sample. Transient absorption kinetics were obtained by detecting probe intensity with/without pump with a Si diode and a WaveMaster 804Zi LeCroy oscilloscope.

2.5. Scanning electron microscopy (SEM) imaging

A Zeiss Supra 40 Scanning Electron Microscope working in optimized low voltage conditions (accelerating voltage <2 kV) was used to image uncoated PIF-Aryl:PDI and TFB/PIF-Aryl:PDI systems. Samples for SEM were deposited on glass/ITO substrates by following a protocol

identical to that for the fabrication of the OPV devices. In order to minimize charging, instead of the typical Al pads used for OPV, the full top surface was evaporated with Al and further grounded by means of Ag conductive paste. Cross-sectional SEM images were recorded after carefully fragmenting the samples; a high accuracy diamond-knife was used for cutting the samples in two pieces and for forming sharp edges that could be examined by SEM. Top SEM images were acquired in an observation angle of 30 degrees on areas of the samples where no metallization with Al had occurred.

2.6. Contact Angle measurements

Contact angle measurements were performed on the surfaces of the studied films using a drop shape analysis system of Dataphysics Instrument OCA 15EC.

2.7. Electrochemical characterization

The highest occupied molecular orbital energy of the polymer studies were determined based on electrochemical measurements. The electrochemical experiments were carried out in argon-purged CH_3CN (Romil Hi-Dry^{TM}) solutions at room temperature with an EcoChemie Autolab 30 multipurpose instrument interfaced to a personal computer. The working electrode was a Pt plate of 0.36 cm^2 of area; the counter electrode was a Pt spiral and a silver wire was employed as a quasi-reference electrode (QRE). The potentials reported are referred to SCE by measuring the AgQRE potential with respect to ferrocene (+0.395 V vs SCE). The compounds examined was deposited on the working electrode via drop casting procedure from a 5×10^{-4} M solution of $CHCl_3$; 0.1 M tetraetylammonium hexafluorophosphate ($TEAPF_6$) was added as supporting electrolyte. Cyclic voltammograms were obtained with scan rates in the range 0.05 – 5 V s^{-1}. The experimental error on the potential values was estimated to be ± 10 mV.

3. Results

Fig. 1a depicts the chemical structure of the materials used in the study. Chart 1 visualizes the energetic alignment of the higher occupied molecular orbitals (HOMO) and lower unoccupied molecular orbitals (LUMO) of the studied materials. The energy of the HOMO and the LUMO levels of PDI is −6.1 eV and −3.8 eV, respectively [9]. The energy of the HOMO and LUMO levels of TFB is at −5.16 eV and −2 eV respectively [18]. Cyclic voltammetry and UV-Vis absorption measurements of a similar poly(indenofluorene) derivative with octyl-side chains [31] find that the LUMO level of PIFs is located at −2.9 eV and the energy of the HOMO level is determined to be −5.7 eV.

3.1. Time-integrated UV-Vis and photoluminescence spectroscopy

Fig. 1b presents the absorption spectra of the TFB layer together with the absorption spectra of the annealed PIF-Aryl:PDI and TFB/PIF-Aryl:PDI films.

The absorption peak of TFB covers the spectral range between 320 – 430 nm and it peaks at 390 nm. The UV-Vis spectrum of the TFB/PIF-Aryl:PDI blend film is a superposition of the absorption spectrum of the TFB interlayer with the absorption spectrum of the PIF-Aryl:PDI system. The latter comprises the absorption peak of PIF-Aryl at 425 nm and the typical absorption band of PDI in the spectral range of 450 – 600 nm. The solid state absorption spectra for films of PIF-Aryl and of PDI dispersed in the inert matrix of poly(styrene) (PS) are given in the **Supporting Information** section. UV-Vis absorption spectroscopy and atomic force microscopy imaging have confirmed the durability of the TFB interlayer on the subsequent spin-coating process that is required for the fabrication of the bilayer system (See **Supporting Information**).

We have evaluated the dissociation efficiency of the PDI excited states at the PIF-Aryl/PDI interface by comparing the photoluminescence (PL) intensity of PDI in a PS:PDI sample with the PL intensity of PDI in a PIF-Aryl:PDI blend film. Fig. 1c depicts the PDI PL spectra of the PS:PDI and the PIF-Aryl:PDI blend films, both containing the same PDI content of 60 wt%; based on the spectral integral of the PDI PL in the spectral region of 565 nm – 750 nm we have determined the PDI PL quenching efficiency to be in the order of 95%. Previous PL quenching studies of polymer:PDI blends have shown that the spectral integrals of the PDI emission are proportional to the quantum efficiency of the PDI luminescence as determined with the use of an integrating sphere [9]. The high PL quenching efficiency indicates a very efficient dissociation step of the excited states in PDI. By adding the TFB interlayer the PL quenching efficiency of PDI in the TFB/PIF-Aryl:PDI bilayer system remained unchanged suggesting that the addition of the TFB layer is not influencing the excited states of PDI.

In order to identify whether charge transfer reactions take place at the TFB/PDI interface of the TFB/PIF-Aryl:PDI bilayer we have performed additional time-integrated PL experiments by directly photoexciting TFB at 390 nm. Fig. 2 present the PL spectra of the TFB interlayer alone together with the PL spectra of the TFB/PIF-Aryl:PDI system before and after the annealing step. The TFB layer alone exhibits the characteristic TFB emission in the spectral range of 410 – 490 nm together with the typ-

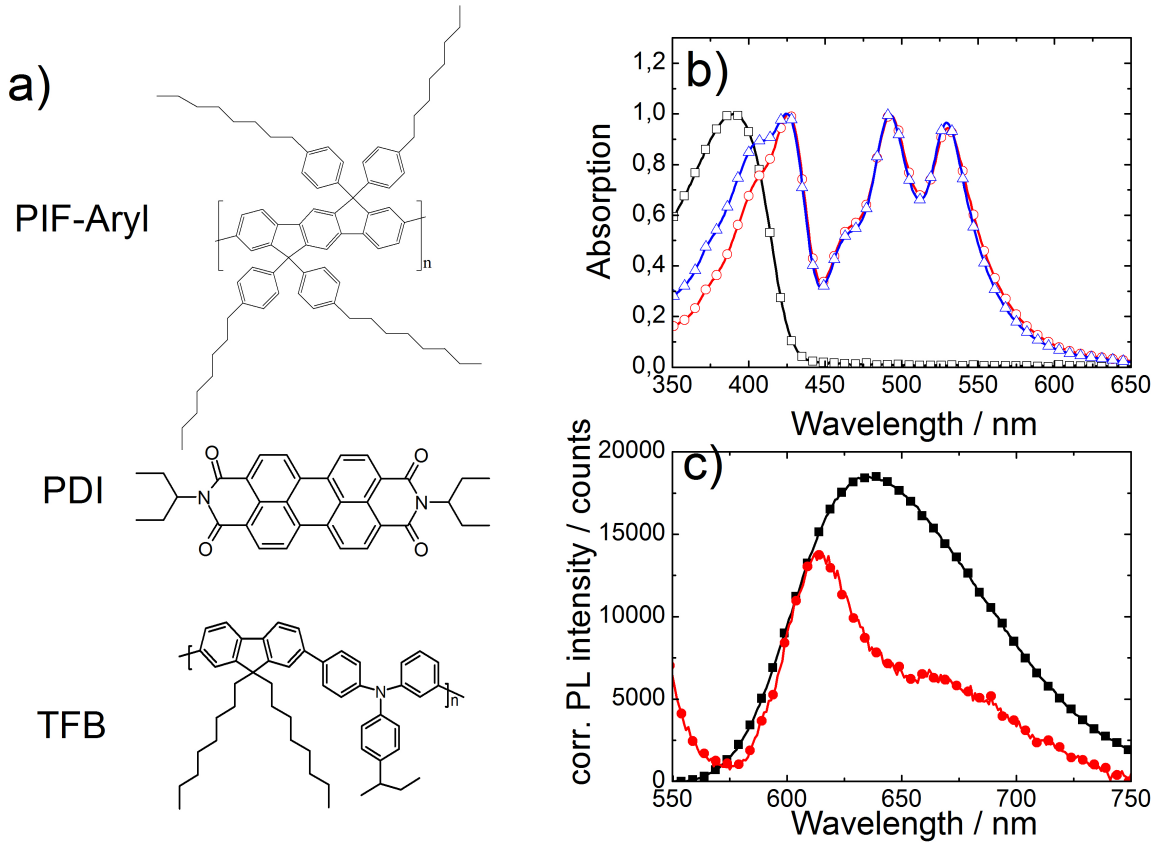

Fig 1. a) The chemical structure of the materials used for this study, b) Normalized UV-Vis absorption spectra of the TFB blocking layer (black open squares) the annealed PIF-Aryl:PDI layer (red open circles) and the annealed TFB/PIF-Aryl:PDI bilayer (blue open triangles), c) PL spectra of a PS:PDI annealed film (black filled squares) and of a PIF-Aryl:PDI annealed film (red filled circles) after photoexcitation at 530 nm. A factor of 10 has been applied for reducing the PL intensity of the PS:PDI film. All PL spectra are corrected for the absorption of the films at the wavelength of photoexcitation.

ical defect PL band that is common in the class of poly- and oligo(para-phenylene)s in the spectral range of 530 – 550 nm [37–40]. The PL quenching of the TFB emission in the bilayer systems may not be due to a charge transfer reaction of the TFB excitons at the TFB/PIF-Aryl:PDI interface. Based on the classical Förster theory [41] we have deduced the Förster distance for the TFB/PDI system to be $R_0 = 4.5$ nm; that is 3/4s of the TFB layer nominal thickness. Therefore, apart from the possibility of a charge transfer reaction with PDI or/and the PIF-Aryl components, there is a probability that the TFB excitons may undergo a resonant energy transfer step from TFB to PDI via a long-range dipole-dipole interaction mechanism.

In comparison with the PL intensity of the TFB layer, the PL quenching efficiency of the TFB excitons in the TFB/PIF-Aryl:PDI bilayer is determined to be 86% before the thermal annealing step but it reduces down to 32% after annealing. The significant recovery of the TFB emission is not followed by a reduction of the PDI emission, as it would have been expected in the case of a resonant energy transfer mechanism between TFB and PDI. On the contrary, the PDI spectral integral between 575 – 695 nm is found to increase by a factor of four after the annealing step. We therefore suggest that the process of energy transfer between the TFB interlayer and the PDI component of the PIF-Aryl:PDI overlayer is negligible and that TFB excitons are more likely to charge transfer at the TFB/PIF-Aryl:PDI interface albeit weakly.

3.2. External quantum efficiency and photoluminescence quenching efficiency

Fig. 3a compares the external quantum efficiency (EQE) spectra of devices based on an annealed single PIF-Aryl:PDI layer and an annealed TFB/PIF-Aryl:PDI bilayer. The single layer device exhibits a maximum EQE value of ~22% peaking at 494 nm. With the addition of the TFB interlayer, the EQE spectrum of the bilayer de-

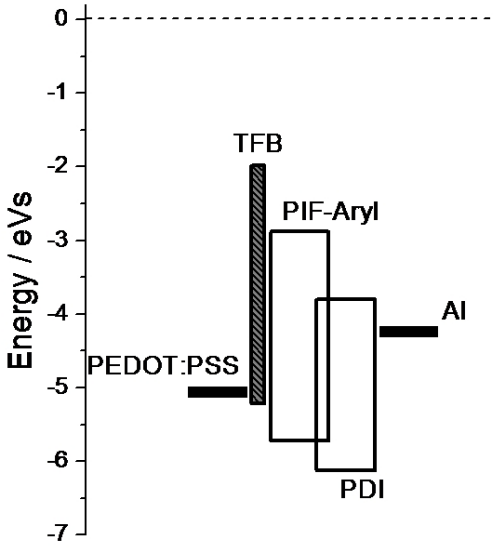

Chart 1. The HOMO and LUMO energy level allignement of the materials used in this study.

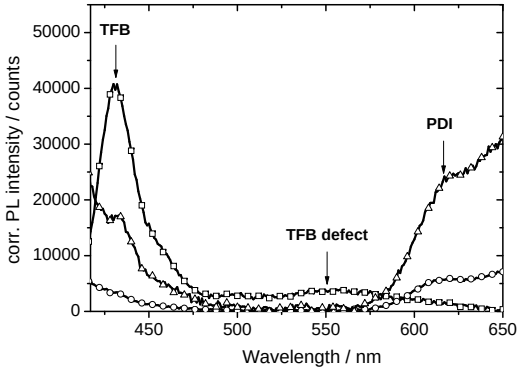

Fig. 2. PL spectra of a TFB layer (squares), a TFB/PIF-Aryl:PDI layer before thermal annealing (circles) and a TFB/PIF-Aryl:PDI layer after thermal annealing (triangles). All layers were deposited on quartz substrates and photoexcitation was at 390 nm.

vice is improved and a maximum EQE value of ~28% is achieved at 493 nm. Not much improvement is seen in the EQE spectra of the bilayer in the spectral region of 350 – 390 nm; in comparison with the single layer device only a marginal increase of 10% is observed for the EQE of the bilayer device at 355 nm.

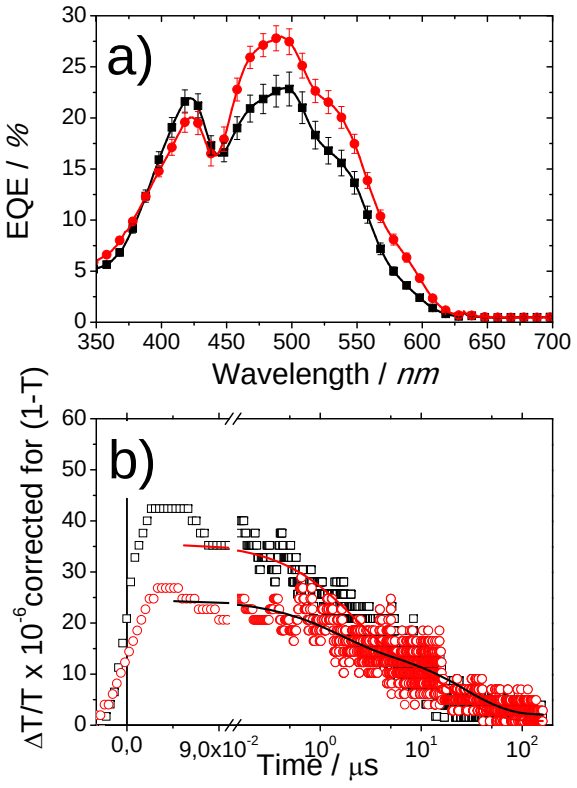

Fig. 3. a) External quantum efficiency spectra of single layer solar cells of PIF-Aryl:PDI (filled squares) and of bilayer solar cells of TFB/PIF-Aryl:PDI (filled circles). For all devices glass/ITO/PEDOT:PSS and Al were the hole-collecting (bottom) and electron-collecting (top) electrodes, respectively, b) transient absorption decays of the 980 nm region of the two systems PIF-Aryl:PDI (open black squares) and TFB/PIF-Aryl:PDI (open red squares). The solid lines are bi-exponential fits to the TA data of the single layer (red solid line) and to the bilayer (black solid line).

3.3. Continuous-wave photo-induced absorption and μs-transient absorption characterization

In order to address whether thermal annealing affects the process of charge recombination and transport in the TFB/PIF-Aryl:PDI bilayer we have performed transient absorption (TA) measurements in annealed samples of PIF-Aryl:PDI and TFB/PIF-Aryl:PDI films, after photoexciting the samples at 355 nm with a repetition rate of 970 Hz. In particular we aimed to examine if the insertion of the TFB interlayer can lead to modifications in the morphology of the carrier-transporting domains in the PIF-Aryl:PDI layer, which would influence charge transport and recombination.

For identifying which spectral region should be monitored for studying the evolution of the photogenerated charged species we have first performed continuous-wave (cw) photoinduced absorption (PIA) measurements in a set of dif-

ferent single layer and bilayer samples (see **Supporting Information** section). For the case of a TFB/PIF-Aryl:PDI film a PIA band was detected in the spectral region of 980 nm after photoexcitation at 532 nm where only the PDI component absorbs. This spectral feature was observed also after photoexcitation of the PIF-Ary:PDI bilayer at 405 nm. Control cw-PIA experiments on single PIF-Aryl and TFB layers, after photoexcitation at 405 nm, and on single PS:PDI layer, after photoexcitation at 532 nm did not reveal any photo-induced absorption band in the spectral region of 980 nm. Moreover, previous reports in the literature suggest that the PDI anion exhibits photoinduced absorption bands at 708 nm and 775 nm [42]. Therefore, we assign the TA band in the region of 980 nm to PIF-Aryl cations that are formed in the PIF-Aryl:PDI composite system after photoexcitation at either wavelengths of 532 nm or 405 nm. Previous PL quenching studies of similar PDI-based bulk heterojunctions have shown that the direct photoexcitation of the PDI component leads to the PDI exciton dissociation and PDI- anion formation via a photo-induced hole transfer between the PDI and polymer HOMO levels [9, 30, 43].

Fig. 3b presents the TA decay transients of the TA intensity at 980 nm of the two systems PIF-Aryl:PDI and TFB/PIF-Aryl:PDI in a time window of 100 μs together with the biexponential fits, after correcting the TA intensity for the absorptance (1-T) of each system at the photoexcitation wavelength of 355 nm. We have chosen to study the dynamics in the low excitation regime in order to minimize sub-microsecond bimolecular recombination processes. In this way most of the recombination occurs in the time window compatible with the temporal resolution provided by our experimental setup. From power dependent TA measurements we have ensured that TA signal has not reached saturation regime at power levels of 540 μW, as it would be expected if it were strongly influenced by sub-μs bimolecular recombination.

In Fig. 3b it can be seen that the addition of the TFB interlayer reduces the apparent charge photogeneration yield in the *ns* time scale. This observation is rationalized as a consequence of the optical filtering effect caused by the TFB interlayer that partially absorbs the photoexcitation light but does not contribute to charge photogeneration. PL quenching experiments in the PIF-Aryl:PDI and TFB/PIF-Aryl:PDI films confirmed that the PL quenching efficiency of the PDI luminescence is also reduced in the bilayer system when photoexcited at 390 nm.

Based on the fitting results of the TA kinetics that are presented in Table 1 it is found that charge recombination can be expressed by short-lived and long-lived charges. No power-law decay could reproduce the experimental TA traces as it is usually observed for the case of non-geminate recombination kinetics of organic photovoltaic blend films in the μs – ms time scale. This may be due to the fact that our measurements monitor a regime with low charge density and in a restricted temporal window.

In the single PIF-Aryl:PDI layer the fraction of the charges that recombines in relative fast time scales is the predominant component of the TA decay suggesting optimized organization of the PIF-Aryl polymer chains and low content of structural traps in the single layer that allow for optimized charge transport and prompt charge recombination losses [44]. By adding the TFB interlayer, the fraction of the long-lived charges increases significantly indicating that charge transport slows down and that the PIF-Aryl chains are less organized containing more structural traps that lead to slow charge recombination kinetics. The structural re-organization of the PIF-Aryl matrix that is implied by the increased fraction of the long-lived charges in the bilayer does not seem to affect the dissociation efficiency of the PDI excited states that lead to charge photogeneration. After the direct generation of the emissive excited state of PDI upon photoexcitation at 530 nm, the quenching efficiency of the PDI luminescence in the PIF-Aryl:PDI and TFB/PIF-Aryl:PDI systems remains virtually unaltered indicating that the suggested structural changes in the PIF-Aryl are not affecting the size of the PDI domains in respect to diffusion length of the PDI emissive state. Table A1 in the **Supporting Information** section summarizes the dissociation efficiency of the PDI excited state in the single layer and bilayer system, for two different wavelengths of photoexcitation at 390 nm and 530 nm. For reference purposes the EQE values at these wavelengths are also given. The corresponding PL spectra are also presented therein.

3.4. Solar cell device characterization

Fig. 4a present the photocurrent density–voltage characteristics of the single layer PIF-Aryl:PDI and bilayer TFB/PIF-Aryl:PDI solar cell devices when recorded under simulated solar light of 0.92 Sun (AM1.5G) and Table 2 summarizes the main device figures of merit of the studied devices.

The single layer device exhibits a PCE value of 0.37% and the insertion of the TFB interlayer increases further the power generation efficiency of the TFB/PIF-Aryl:PDI bilayer device, resulting in a PCE value of 0.58%. Fig. 4b presents the dark current density-voltage characteristics of the single layer PIF-Aryl:PDI and bilayer TFB/PIF-Aryl:PDI solar cell devices. It is found that both in the case of the forward and reverse bias operation the dark current (I_d) of the bilayer device is reduced.

Table 1. Fitting results of the bi-exponential fits applied on the TA data of Fig. 3b.

System	Baseline	A_1 (a.u.)	τ_1 (μs)	A_2 (a.u.)	τ_2 (μs)	adj. Rsquare
Single Layer PIF-Aryl:PDI	0.021 ± 0.001	0.381 ± 0.005	19.5 ± 0.4	0.461 ± 0.006	1.7 ± 0.045	0.924
Bilayer TFB/PIF-Aryl:PDI	0.078 ± 0.003	0.499 ± 0.005	26.9 ± 0.8	0.344 ± 0.011	1.36 ± 0.08	0.816

Table 2. The main performance parameters of the single and bilayer solar cell devices extracted by the J-V curves of Fig. 4a.

OPV device structure	V_{oc} (Volts)	J_{sc} (mA cm^{-2})	FF (%)	PCE (%)	R_{SH} (kΩ)	R_S (kΩ)
PEDOT/PIF-Aryl:PDI/Al	0.7 ± 0.011	1.62 ± 0.017	30.0 ± 0.63	0.37 ± 0.007	66.2 ± 1.4	1.0 ± 0.02
PEDOT/TFB/PIF-Aryl:PDI/Al	0.87 ± 0.012	2.1 ± 0.11	32.8 ± 0.45	0.58 ± 0.043	98.4 ± 0.3	1.3 ± 0.02

3.5. Contact angle characterization and scanning electron microscopy imaging

Scanning electron microscopy (SEM) imaging was performed on the PIF-Aryl:PDI and TFB/PIF-Aryl:PDI systems deposited on glass/ITO substrates for confirming the effects of the TFB interlayer on the morphology of the PIF-Aryl:PDI layer, as inferred by the TA results of Fig. 3b. Fig. 5 presents the acquired images of the two systems both on a top-view and a cross-sectional mode. Previous studies on the surface topography of several PDI blend films have shown the general tendency for the formation of PDI ribbon-like features [19, 45]. The difference in the surface texture of the PIF-Aryl:PDI (Fig. 5a) is striking. Based on Fig. 5a and 5b it becomes apparent that the insertion of the TFB interlayer drastically affects the surface morphology of the PIF-Aryl:PDI layer. In the case of the single layer sample (Fig. 5a) a clear formation of whisker-like objects can be observed on the surface of the sample where no Al metal has been deposited. The whiskers are as long as 530 nm, as wide as 70 nm and they are organized in a herringbone-like arrangement. In addition, smaller ribbons can be observed underneath the surface of the whiskers and the nominal length of the ribbons is in the order of 200 nm. The previously worm-like features of PDI are seen only after inserting the TFB interlayer. In the presence of TFB the highly organized whisker-like objects disappear and the ribbons are found to emerge on the sample surface out of an amorphous matrix (Fig. 5b).

Fig. 5c presents the SEM image of the PIF-Aryl:PDI sample where the structure of ITO/PEDOT:PSS/PIF-Aryl:PDI is seen. Similarly, the SEM cross-sectional images resolves the stratified structure ITO/PEDOT:PSS/TFB/PIF-Aryl:PDI of the bilayer shown in Fig. 5d.

Previous AFM studies on PDI-based blends have shown that PDI tends to form ribbon-like structure on the surface of PDI-containing polymeric composites. In our PIF-Aryl:PDI layer, underneath the surface of the whiskers (Fig. 5a), PDI forms ribbons that are much alike in structure with those previously observed [9, 18]. Therefore, it is unlikely that the whiskers that are found on the surface of the PIF-Aryl:PDI single layer system are made of PDI. Previous wide-angle X-ray scattering (WAXS) studies on microextruded fibers and atomic force microscopy (AFM) imaging characterization on as-spun and annealed films of PIF-Aryl [31] have suggested that in the solid state the macromolecular fragments of PIF-Aryl are organized locally in amorphous arrangements that form elongated rod-shaped aggregates. At this stage the SEM images cannot provide information about the purity of the observed whiskers and in the light of the previous WAXS and AFM findings we assign them on the mesoscopic organization of PIF-Aryl aggregates. The thickness of the surface that is formed by the PIF-Aryl whiskers must be very small. The cross-sectional image in Fig. 5c is taken for a sample area where the Al metal was unintentionally peeled off and the removal of Al also removed the thin whisker surface, leaving exposed the PDI ribbons on the surface. The fact that no whisker formation is observed in the case of the TFB/PIF-Aryl:PDI layer (Fig. 5b) suggests that the addition of the TFB layer prevents the organization of the PIF-Aryl component and promotes the emergence of the PDI on the surface out from the amorphous PIF-Aryl matrix.

We have further performed contact angle measurements in a set of samples (Fig. 6) for elucidating whether the insertion of the TFB interlayer can indirectly lead to modified surface properties in the studied systems. In particular with the drop analysis technique we have determined the contact angle in layers of glass/TFB, glass/PIF-Aryl, glass/PS and glass/PS:PDI. For reference purposes the contact angle of the glass/ITO/PEDOT:PSS sample was also measured. Table 3 presents the determined contact

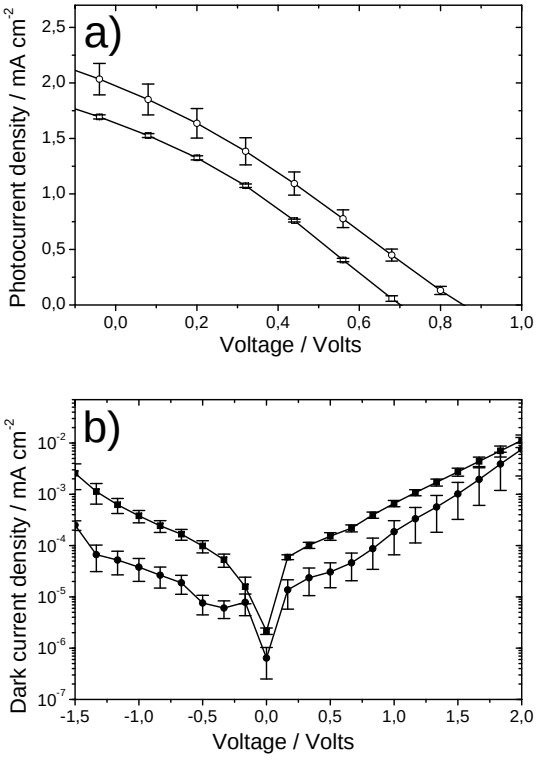

Fig. 4. a) Photocurrent J-V curves for single layer solar cells of annealed PIF-Aryl:PDI (open squares) and for bilayer solar cells of annealed TFB/PIF-Aryl:PDI (open circles). b) Dark current J-V curves for single layer solar cells of annealed PIF-Aryl:PDI (filled squares) and for annealed bilayer solar cells of TFB/ PIF-Aryl:PDI (filled circles). For all devices glass/ITO/PEDOT:PSS and Al were the hole-collecting (bottom) and electron-collecting (top) electrodes, respectively. Photocurrent metrics were recorded with 0.92 Suns of AM1.5G.

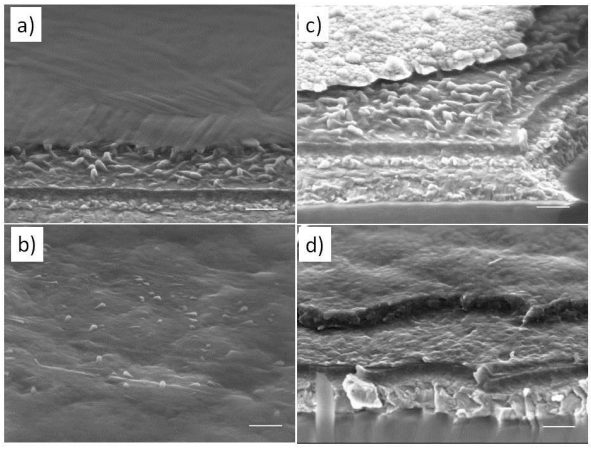

Fig. 5. Top-view SEM images of the a) PIF-Aryl:PDI single layer, b) TFB/PIF-Aryl:PDI bilayer and cross-sectional SEM images of the c) PIF-Aryl:PDI single layer, d) a TFB/PIF-Aryl:PDI bilayer.

angle values for these samples.

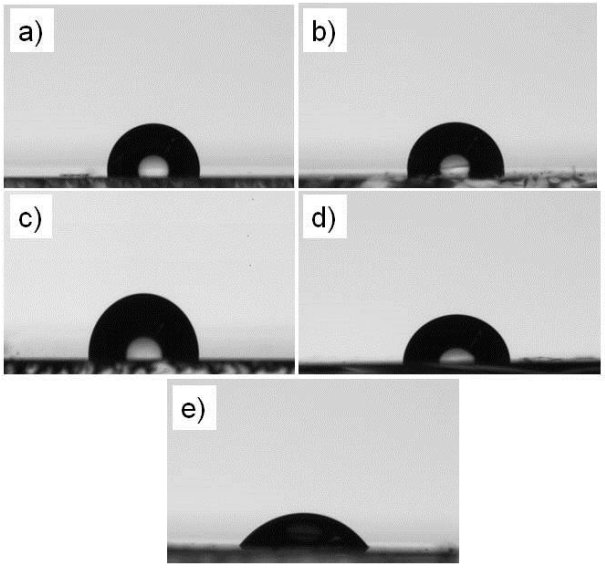

Fig. 6. Water droplets on layers of a) glass/TFB, b) glass/PIF-Aryl, c) glass/PS, d) glass/PS:PDI 60 wt% and e) glass/ITO/PEDOT:PSS.

Table 3. Contact angle values as determined by the drop shape analysis for the studied organic layers (Fig. 6).

Sample	Contact angle (°)
glass/TFB	99.8
glass/PIF-Aryl	98.3
glass/PS	93.8
glass/PS:PDI 60 wt%	86.4
glass/ITO/PEDOT:PSS	52.6

From all measured samples the lowest contact angle value is obtained for the PEDOT:PSS layer confirming the strongest hydrophilic character of this layer amongst all characterized samples. In contrast, the TFB, PIF-Aryl and PS polymeric matrices were found more hydrophobic with contact angle values higher than 90°. Interestingly, the addition of the 60 wt% PDI component in the PS matrix reduces the hydrophobic character of the PS:PDI composite layer thus increasing the affinity of the PS:PDI layer to the PEDOT:PSS.

4. Discussion

Despite the non-optimized absorption properties of the PIF-Aryl polymeric matrix, both single layer and bilayer devices of PIF-Aryl:PDI combination exhibit power conversion efficiencies that are drastically improved in re-

spect to previous PCEs obtained by other polymeric PDI OPV composites of the same PDI derivative [9, 18]. Impressively, the obtained 0.58% PCE value of the TFB/PIF-Aryl:PDI system is higher than the PCE reported for OPV devices based on poly(hexyl-thiophene):PDI composites of a bay-substituted PDI derivative prepared by a synthetic protocol that required more reaction steps [46].

Compared to the single layer device, all device metrics of the bilayer device are found optimized (Table 2). The use of the TFB interlayer is positively affecting the PCE of the TFB/PIF-Aryl:PDI solar cell and relatively to the single layer PIF-Aryl:PDI device it results in an increased PCE by more than 55%. In respect to the single layer PIF-Aryl:PDI system, the I_{sc} of the TFB/PIF-Aryl:PDI bilayer device is found to increase by 29% whereas a significant improvement of more than 20% is found also in the V_{oc} parameter [14, 15]. In the bilayer device I_d is found significantly reduced in respect to the I_d of the single layer PIF-Aryl:PDI device (Fig. 4b). The observed reduction cannot be attributed to a different electric field that could arise by differences in the total thickness of the device layer that is sandwiched between the PEDOT:PSS and Al electrodes. For the single layer device the PIF-Aryl:PDI layer was 97 ± 0.7 nm thick whereas for the case of the bilayer device a 7.8 ± 0.6 nm thick TFB layer was used making the total thickness of the TFB/PIF-Aryl:PDI layer 101.4 ± 0.7 nm. Table 2 shows that the shunt resistance is increased for the case of the bilayer device. In the forward bias dark current, electron injection takes place from the metal cathode to the LUMO levcel of PDI. The injected electrons recombine at the PDI/PEDOT:PSS interfaces. Similarly, hole injection takes place from the PEDOT:PSS to the HOMO level of PIF-Aryl component and hole recombination may take place at the PIF-Aryl/Al interfaces. The reduced dark current of the bilayer device in the forward bias suggests a reduction of the PEDOT:PSS/PDI and PIF-Aryl/Al interfaces. This modification of the layer morphology is achieved with the use of a purely solution-based processing protocol [17, 18] without the requirement of cross-linking for the fabrication of the bilayer optoelectronic medium of the TFB/PIF-Aryl:PDI system.

It is meaningful to comment on the dark J-V characteristics of Figure 4. The lack of rectification and the symmetry of the J-V curves for negative and positive voltages indicate poor diode behaviour. In combination with the low fill factor values that are given in Table 2, these findings suggest that one of the factors that limit the device performance of PDI-based organic solar cells is the inefficient charge extraction. In another work we have demonstrated how the fill factor of a PDI-based solar cell can improve when the surface roughness of the photoactive layer is reduced and consequently when the interface of the photoactive layer and the top electrode is optimized [47]. The subject of charge extraction efficiency in PDI-based OPVs will be addressed separately based on transient photocurrent studies.

In line with the increased I_{sc}, the EQE of the bilayer device is much improved in respect to the EQE of the single PIF-Aryl:PDI device (Fig. 3a). Interestingly, the observed improvement in the EQE takes place between 450 – 620 nm, in the spectral region where the PDI component alone absorbs light. The minor increase in the EQE at shorter wavelengths in the region where the TFB excitons absorb indicate that despite the occurrence of charge transfer reactions between TFB interlayer and the PIF-Aryl:PDI top-layer, the electronic coupling of TFB layer and the active layer remains weak and no significant photocurrent generation at short wavelengths is observed in the bilayer device. This is in contrast to what has been proposed for the impact of polymeric interlayers in fullerene-based solar cells [28]. We note that in our experiments the thickness of the TFB interlayer is four times smaller than the interlayer thickness used in [28]. In addition, the chemical structure of the photoactive materials used in our study is different than those used in [28].

The increase in the EQE of the bilayer device at longer wavelengths cannot be attributed to a higher dissociation yield of the PDI emissive excited state in the TFB/PIF-Aryl:PDI system since no difference was found in the PL quenching efficiency between the PIF-Aryl:PDI and TFB/PIF-Aryl:PDI systems after photoexcitation at 530 nm. Moreover, based on the TA and SEM results it is found that the insertion of the TFB interlayer induces the reorganization of the PIF-Aryl component in the PIF-Aryl:PDI top layer, leading to slower charge recombination kinetics and consequently to slower charge transport. Therefore the observed improvement in the photocurrent of the bilayer device should be the result of an optimized charge extraction that is assisted by the changes in the morphology of the PIF-Aryl:PDI top layer of the bilayer and by the re-distribution of the PIF-Aryl and PDI components along the TFB and Al boundaries of the device. The increased fill factor of the bilayer device is also in favour of the notion that charge extraction is improved. However more evidence in support of our suggestion comes from the contact angle measurement study (Table 3). TFB and PS are found to form equally hydrophobic surfaces. Moreover, the addition of PDI in a PS film reduces the hydrophobicity of the PS:PDI film and suggests that PDI is more hydrophilic than PS. Therefore, after the insertion of the TFB interlayer, the PDI component is likely to be repelled away by the TFB interlayer towards the surface/air interface whereas the PIF-Aryl component will be more evenly distributed across the top layer of PIF-

Aryl:PDI due to its higher compatibility with the TFB interlayer. Consequently by inserting the TFB interlayer the PDI and PIF-Aryl components are re-distributed as such so that they are homogeneously dispersed along the device electrodes with PIF-Aryl to be more compatible with the TFB and the PDI to gain accessibility to the electron-collecting electrode of Al. Under these conditions the carrier-transporting components are well placed in respect to the corresponding carrier-collecting contacts of the device and the extraction of the photogenerated carriers is enhanced.

5. Conclusion

In conclusion, we have presented a methodology for the fabrication of a non-fullerene-based bilayer OPV device with an improved PCE parameter. In particular, we have managed to increase the PCE parameter of a perylene diimide-containing OPV system by more than 1.5 times after inserting the electro-optically active TFB interlayer between the hole-collecting electrode PEDOT:PSS and the PIF-Aryl:PDI photoactive layer of the device.

The utilized TFB interlayer induces the re-distribution of the PDI and PIF-Aryl components of the photoactive layer along the direction of the device contacts, thus optimizing the connectivity of the electron-transporting component in the photoactive layer with the corresponding electron-collecting electrode of the device. As a result of the component re-organization the I_{sc} parameter of the device improves greatly.

At this stage the preparation protocol of the TFB interlayer requires further research in terms of the basic ink parameters such as viscocity and surface tension. The optimation of the ink properties is expected to simplify the fabrication of bilayer OPV devices with optimized morphologies by means of roll-to-roll large area deposition techniques [48].

Acknowledgements

PEK acknowledges the financial support of a Marie Curie Intra European Fellowship (FP7-PEOPLE-2011-IEF project DELUMOPV). J.C-G and M.M.M. acknowledge financial support from the Spanish Ministry of Economy and Competiveness (contracts RYC 2009-05475 and TEC2010-21830-C02-02) and FP7-PEOPLE-2007-2-3-COFUND Amarout program, respectively.

References

[1] G. Li, R. Zhu and Y. Yang, Polymer solar cells, *Nature Photonics*, 2012, **6**, 153-161.

[2] G. Dennler, M. C. Scharber and C. J. Brabec, *Advanced Materials*, 2009, **21**, 1323-1338.

[3] Z. C. He, C. M. Zhong, X. Huang, W. Y. Wong, H. B. Wu, L. W. Chen, S. J. Su and Y. Cao, *Advanced Materials*, 2011, **23**, 4636.

[4] Y. Y. Liang, Z. Xu, J. B. Xia, S. T. Tsai, Y. Wu, G. Li, C. Ray and L. P. Yu, *Advanced Materials*, 2010, **22**, E135-E138.

[5] E. J. Zhou, M. Nakamura, T. Nishizawa, Y. Zhang, Q. S. Wei, K. Tajima, C. H. Yang and K. Hashimoto, *Macromolecules*, 2008, **41**, 8302-8305.

[6] C. H. Woo, P. M. Beaujuge, T. W. Holcombe, O. P. Lee and J. M. J. Frechet, *Journal of the American Chemical Society*, 2010, **132**, 15547-15549.

[7] J. Peet, J. Y. Kim, N. E. Coates, W. L. Ma, D. Moses, A. J. Heeger and G. C. Bazan, *Nature Materials*, 2007, **6**, 497-500.

[8] A. C. Arias, J. D. MacKenzie, R. Stevenson, J. J. M. Halls, M. Inbasekaran, E. P. Woo, D. Richards and R. H. Friend, *Macromolecules*, 2001, **34**, 6005-6013.

[9] P. E. Keivanidis, I. A. Howard and R. H. Friend, *Advanced Functional Materials*, 2008, **18**, 3189-3202.

[10] M. Campoy-Quiles, T. Ferenczi, T. Agostinelli, P. G. Etchegoin, Y. Kim, T. D. Anthopoulos, P. N. Stavrinou, D. D. C. Bradley and J. Nelson, *Nature Materials*, 2008, **7**, 158-164.

[11] A. C. Arias, N. Corcoran, M. Banach, R. H. Friend, J. D. MacKenzie and W. T. S. Huck, *Applied Physics Letters*, 2002 **80**, 1695-1697.

[12] M. Vogel, J. Strotmann, B. Johnev, A. C. Lux-Steiner and K. Fostiropoulos, *Thin Solid Films*, 2006, **511**, 367-370.

[13] Ohkita H., Cook S., Astuti Y., Duffy W., Tierney S., Zhang W., Heeney M., McCulloch I., Nelson J., Bradley D. D. C. and Durrant J. R., *Journal of the American Chemical Society*, 2008, **130**, 3030.

[14] A. W. Hains, T. J. Marks, *Applied Physics Letters*, 2008, **92**, 023504.

[15] N. Li, B. E. Lassiter, R. R. Lunt, G. Wei and S. R. Forrest, *Applied Physics Letters*, 2009, **94**, 023307.

[16] P. Sonar, J. Pui Fong Lim K. Leok Chan, *Energy & Environmental Science*, 2011, **4**, 1558-1574

[17] C. L. Chochos, N. Tagmatarchis, V. Gregoriou, *The Royal Society of Chemistry Advances*, 2013, doi: 10.1039/C3RA22926B.

[18] P. E. Keivanidis, S. H. Khong, P. K. H. Ho, N. C. Greenham and R. H. Friend, *Applied Physics Letters*, 2009, **94**, 173303.

[19] P. E. Keivanidis, P. K. H. Ho, R. H. Friend and N. C. Greenham, *Advanced Functional Materials*, 2010, **20**, 3895-3903.

[20] J. H. Seo, A. Gutacker, Y. Sun, H. Wu, F. Huang, Y.

Cao, U. Scherf, A. J. Heeger, G. C. Bazan, *Journal of the American Chemical Society*, 2011, **133**, 8416-8419.
[21] R. Steim, F. R. Kogler, C. J. Brabec, *Journal of Materials Chemistry*, 2010, **20**, 2499-2512.
[22] R. Steim, S. A. Choulis, P. Schilinsky, C. J. Brabec, *Applied Physics Letters*, 2008, **92**, 093303.
[23] J. Subbiah, D. Y. Kim, M. Hartel, F. So, *Applied Physics Letters*, 2010, **96**, 063303.
[24] S. H. Park, A. Roy, S. Beaupré, S. Cho, N. Coates, J. S. Moon, D. Moses, M. Leclerc, K. Lee, A. J. Heeger, *Nature Photonics*, 2009, **3**, 297.
[25] Z. He, C. Zhong, S. Su, M. Xu, H. Wu, Y. Cao, *Nature Photonics*, 2012, **6**, 591-595.
[26] Y. Zhou, C. F.-Hernandez, J. Shim, J. Meyer, A. J. Giordano, H. Li, P. Winget, P. Papadopoulos, H. Cheun, J. Kim, M. Fenoll, A. Dindar, W. Haske, E. Najafabadi, T. M. Khan, H. Sojoudi, S. Barlow, S. Graham, J.-L. Brédas, S. R. Marder, A. Kahn, B. Kippelen, *Science*, 2012, **336**, 327-332.
[27] Z. Tang, L. M. Andersson, Z. George, K. Vandewal, K. Tvingstedt, P. Heriksson, R. Kroon, M. R. Andersson, O. Inganäs, *Advanced Materials*, 2012, **24**, 554-558.
[28] F. Deschler, D. Riedel, B. Ecker, E. von Hauff, E. Da Como and R. C. I. MacKenzie, *Physical Chemical Physical*, 2013, 15, 764-769.
[29] J. J. Dittmer, E. A. Marseglia, R. H., Friend, *Advanced Materials*, 2000, **12**, 1270.
[30] I. A. Howard, F. Laquai, P. E. Keivanidis, R. H. Friend, N. C. Greenham, *The Journal of Physical Chemistry C*, 2009, **113**, 21225.
[31] P. E. Keivanidis, J. Jacob, L. Oldridge, P. Sonar, B. Carbonnier, S. Baluschev, A. C. Grimsdale, K. Müllen and G. Wegner, *ChemPhysChem*, 2005, **6**, 1650.
[32] J. Jacob, J. Y. Zhang, A. C. Grimsdale, K. Müllen, M. Gaal and E. J. W. List, *Macromolecules*, 2003, **36**, 8240-8245.
[33] F. Laquai, P. E. Keivanidis, S. Baluschev, J. Jacob, K. Müllen and G. Wegner, *Applied Physics Letters*, 2005, **87**, 261917.
[34] R. Singh, E. Giussani, F. Di Fonzo, D. Fazzi, M. M. Mróz, J. Cabanillas-Gonzalez, K. Müllen, J. Jacob, P. E. Keivanidis, (manuscript in preparation)
[35] J. S. Kim, R. H. Friend, I. Grizzi, J. H. Burroughes, *Applied Physics Letters*, 2005, **87**, 023506.
[36] S. A. Choulis, V. E. Choong, M. K. Mathai, F. So, *Applied Physics Letters*, 2005, **87**, 113503.
[37] E. J. W. List, R. Guentner, P. S. de Freitas and U. Scherf, *Advanced Materials*, 2002, **14**, 374-378.
[38] M. Sims, D. D. C. Bradley, M. Ariu, M. Koeberg, A. Asimakis, M. Grell and L. D.G., *Advanced Functional Materials*, 2004, **14**, 765-781.
[39] C. L. Chochos, J. K. Kallitsis, P. E. Keivanidis, S. Baluschev and V.G. Gregoriou, *Journal of Physical Chemistry B*, 2006, **110**, 4657.
[40] J. Kang, J. Jo, Y. Jo, S. Y. Lee, P. E. Keivanidis, G. Wegner and D. Y. Yoon, *Polymer*, 2008, **49**, 5700-5704.
[41] M. Maus, R. De, M. Lor, T. Weil, S. Mitra, U. M. Wiesler, A. Herrmann, J. Hofkens, T. Vosch, K. Müllen and F. C. De Schryver, *Journal of the American Chemical Society*, 2001, **123**, 7668-7676
[42] M. W. Holman, P. Yan, D. M. Adams, S. Westenhoff and C. Silva, *Journal of Physical Chemistry A*, 2005, **109**, 8548-8552.
[43] A. A. Bakulin, J. C. Hummelen, M. S. Pshenichnikov, P. H. M. van Loosdrecht, *Advanced Functional Materials*, 2010, **20**, 1653 - 1660.
[44] M. A. Faist, P. E. Keivanidis, S. Foster, P. H. Wobkenberg, T. D. Anthopoulos, D. D. C. Bradley, J. R. Durrant and J. Nelson, *Journal of Polymer Science Part B-Polymer Physics*, 2011, **49**, 45-51.
[45] L. Schmidt-Mende, A. Fechtenkötter, K. Müllen, E. Moons, R. H. Friend, J. D. MacKenzie, Science 2001, **293**, 1119-1122.
[46] V. Kamm, G. Battagliarin, I. A. Howard, W. Pisula, A. Mavrinskiy, C. Li, K. Müllen, F. Laquai, *Advanced Functional Materials*, 2011, **1**, 297-302.
[47] T. Ye, R. Singh, H.-J. Butt, G. Floudas, P. E. Keivanidis, *submitted manuscript*
[48] F. C. Krebbs, *Solar Energy Materials & Solar Cells*, 2009, **93**, 394-412.

Appendix A: SUPPORTING INFORMATION

1. Improving the layer morphology of solution-processed perylene diimide organic solar cells with the use of a polymeric interlayer

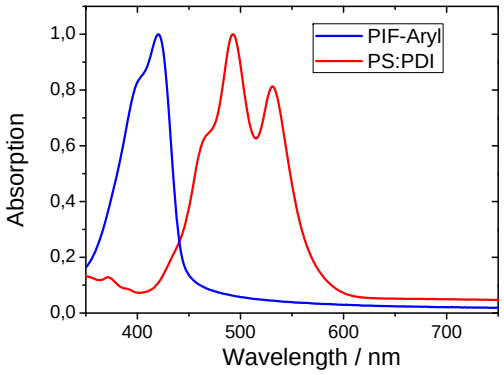

Fig. A1. Normalized UV-Vis linear absorption spectra of a PIF-Aryl film (blue line) and a poly(styrene):PDI (PS:PDI) 60 wt% film. Both layers were deposited on glass substrates.

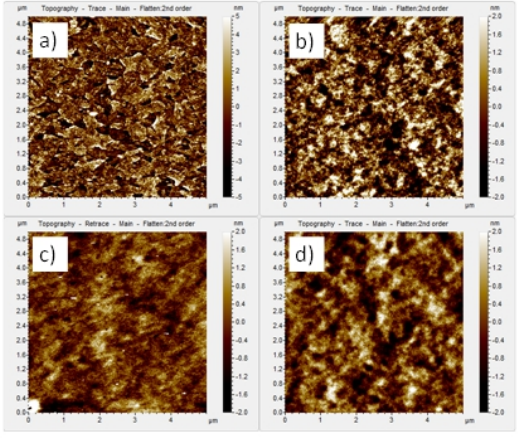

Fig. A2. Tapping mode atomic force microscopy height images for a a) glass/ITO substrate, b) glass/ITO/PEDOT:PSS substrate, c) glass/ITO/PEDOT:PSS/TFB substrate and d) glass/ITO/PEDOT:PSS/TFB after rinsing with chloroform and thermal annealing.

Table A1. Root mean square roughness for the surfaces of the films presented in Fig. A2.

Sample	rms roughness (nm)
Glass/ ITO	2.31
Glass/ ITO/PEDOT:PSS	1.15
Glass/ ITO/PEDOT:PSS/TFB (before rinsing + thermal annealing)	0.79
Glass/ ITO/PEDOT:PSS/TFB(after rinsing + thermal annealing)	0.84

Table A2. Comparison of the film thickness determination results as obtained with the use of surface profilometry ($d_{profilometer}$) and atomic force microscopy (d_{AFM}).

Sample	$d_{profilometer}$ (nm)	d_{AFM} (nm)
Glass/ ITO/PEDOT:PSS	42	40
Glass/ ITO/PEDOT:PSS/TFB (before rinsing + thermal annealing)	12.6	12
Glass/ ITO/PEDOT:PSS/TFB(after rinsing + thermal annealing)	8.1	8

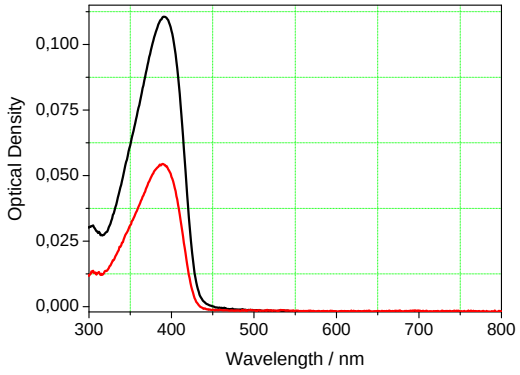

Fig. A3. UV-Vis absorption spectra of a TFB layer before spin-rinsing and thermal annealing (black line) and after spin-rinsing with chloroform and thermal annealing.

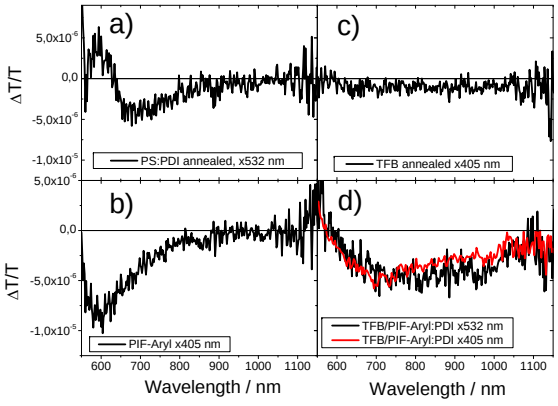

Fig. A4. Cw-photoinduced absorption spectra for a) a PS:PDI film under photoexcitation at 532 nm, b) an annealed PIF-Aryl film under photoexcitation at 405 nm c) an annealed TFB film under photoexcitation at 405 nm and d) a TFB/PIF-Aryl:PDI bilayer under photoexcitation at 405 nm (red line) and at 532 nm (black line). All PDI-containing samples were with 60 wt% PDI. The excitation intensity for 405 nm and 532 nm was 1.3 mW/cm^2 and 1.9 mW/cm^2, respectively.

Table A3. External quantum efficiency (EQE), and PL quenching efficiency (Φ) as determined at two different wavelengths for the annealed PIF-Aryl:PDI and TFB/PIF-Aryl:PDI systems.

Measured property	PIF-Aryl:PDI	TFB/PIF-Aryl:PDI
EQE_{530nm}	16.6% ± 1.3%	21.3% ± 1.1%
Φ_{PDI} ($\lambda_{exc.}$ = 530 nm)	94.7%	94.3%
EQE_{390nm}	13.1% ± 0.6%	12.8% ± 0.4%
Φ_{PDI} ($\lambda_{exc.}$ = 390 nm)	87.2%	85.4%

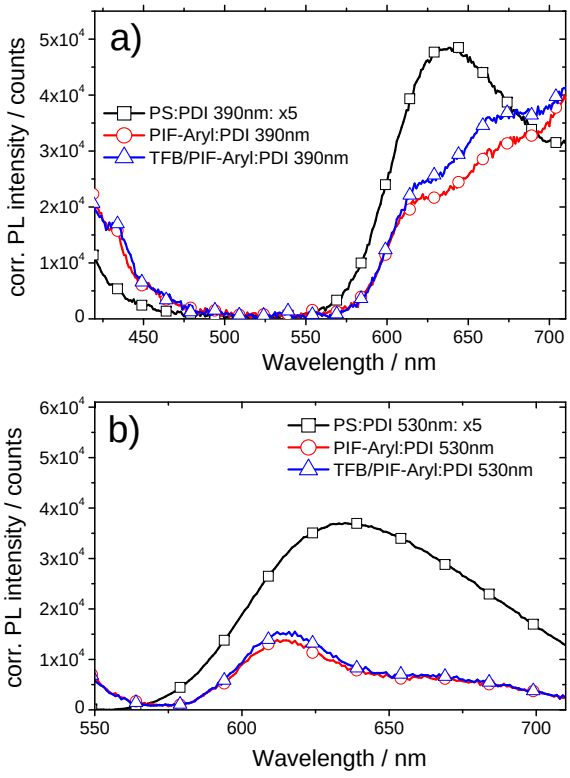

Fig. A5. Room temperature PL spectra of the PS:PDI (squares), PIF-Aryl:PDI (circles) and TFB/PIF-Aryl:PDI (triangles) systems for photoexcitation of the samples at a) 390 nm and b) 530 nm. All films were deposited on quartz substrates and annealed with the same conditions. In all cases the PDI content was 60 wt%.